Available online at www.sciencedirect.com
ScienceDirect
Journal of Power Sources 168 (2007) 379–390
JOURNAL OF POWER SOURCES
www.elsevier.com/locate/jpowsour

Planar and three-dimensional microfluidic fuel cell architectures based on graphite rod electrodes

Erik Kjeang, Jonathan McKechnie, David Sinton *, Ned Djilali

Department of Mechanical Engineering, and Institute for Integrated Energy Systems (IESVic), University of Victoria, P.O. Box 3055 STN CSC, Victoria, BC V8W 3P6, Canada

Received 12 December 2006; received in revised form 1 February 2007; accepted 2 February 2007
Available online 12 March 2007

Abstract

We propose new membraneless microfluidic fuel cell architectures employing graphite rod electrodes. Commonly employed as mechanical pencil refills, graphite rods are inexpensive and serve effectively as both electrode and current collector for combined all-vanadium fuel/oxidant systems. In contrast to film-deposited electrodes, the geometry and mechanical properties of graphite rods enable unique three-dimensional microfluidic fuel cell architectures. Planar microfluidic fuel cells employing graphite rod electrodes are presented here first. The planar geometry is typical of microfluidic fuel cells presented to date, and permits fuel cell performance comparisons and the evaluation of graphite rods as electrodes. The planar cells produce a peak power density of 35 mW cm^{-2} at 0.8 V using 2 M vanadium solutions, and provide steady operation at flow rates spanning four orders of magnitude. Numerical simulations and empirical scaling laws are developed to provide insight into the measured performance and graphite rods as fuel cell electrodes.

We also present the first three-dimensional microfluidic fuel cell architecture with multiple electrodes. The proposed fuel cell architecture, consisting of a hexagonal array of graphite rods, enables scale-up/integration of microfluidic fuel cell technology as well as power conditioning flexibility beyond that of the traditional fuel cell stack. When provided the same flow rate as the planar cell, the array cell generated an order of magnitude higher power output. The array architecture also enabled unprecedented levels of single pass fuel utilization, up to 78%.

Keywords: Microfluidic fuel cell; Membraneless fuel cell; Laminar flow-based fuel cell; Vanadium redox couple; Graphite rod; Array architecture fuel cell

1. Introduction

Technical development and miniaturization efforts in the area of portable electronics have generated unprecedented demand for small and efficient power supplies. The cost tolerance associated with the development of new solutions for small-scale power generation is therefore relatively high [1]. Microstructured fuel cells are considered a technology with the potential to facilitate these accelerating power requirements [2]. Proton exchange membrane (PEM) fuel cells based on hydrogen provide competitive power densities, but the energy density of such fuel cell systems is limited by on-board fuel storage. In general, liquid fuels enable higher energy density than gaseous fuels. Direct methanol fuel cells, for example, are capable of combining relatively high power densities and energy densities [3–5]. There are, however, several challenges associated with these, for instance, methanol crossover through the membrane and slow anode kinetics, which reduce efficiency and open-circuit voltage [6].

Microfluidic fuel cells, also called laminar flow-based fuel cells or membraneless fuel cells, provide an alternative avenue towards miniaturized power supplies. A microfluidic fuel cell is defined here as a device that confines all fundamental components of a fuel cell to a single microstructured manifold. In the case of non-specific catalysts or active sites, such fuel cells exploit the relatively low rates of diffusive mixing inherent to co-laminar microfluidic flow to maintain the separation of anolyte and catholyte streams flowing side-by-side, thereby eliminating the need for a physical barrier such as a membrane [7]. Ionic conduction is facilitated by a supporting electrolyte contained within the reactant streams. Mixing of the two streams occurs by transverse diffusion only, and is restricted to an interfacial width

* Corresponding author. Tel.: +1 250 721 8623; fax: +1 250 721 6051.
E-mail address: dsinton@me.uvic.ca (D. Sinton).

0378-7753/$ – see front matter © 2007 Elsevier B.V. All rights reserved.
doi:10.1016/j.jpowsour.2007.02.087

Nomenclature

a	chemical activity
c	concentration (mol m^{-3})
d	rod diameter (m)
D	solute diffusivity (m^2 s^{-1})
D_h	hydraulic diameter (m)
E	electrochemical potential (V)
E°	standard redox potential (V)
F	Faraday's constant (C mol^{-1})
h	channel height (m)
I	current (A)
J	current density (A m^{-2})
l	active length of rod (m)
n	number of electrons
p	pressure (Pa)
Q	flow rate (m^3 s^{-1})
Q_J	current source (A m^{-3})
R	universal gas constant (J mol^{-1} K^{-1})
R_s	ohmic resistance (Ω)
s	inter-electrode spacing (m)
T	temperature (K)
U	mean velocity (m s^{-1})
V	electric potential (V)
w	Channel width (m)
W	pumping power (W)

Greek letters

η	fuel utilization
μ	dynamic viscosity (kg m^{-1} s^{-1})
σ	electrical conductivity (S m^{-1})

Subscripts

e	electrode
ox	oxidized species
red	reduced species
0	initial value

at the center of the channel. This inter-diffusion zone [8] has an hourglass shape with a maximum width at the channel walls [7]. Anode and cathode are integrated on the walls of the manifold sufficiently far away from the co-laminar inter-diffusion zone in order to prevent fuel crossover. The microfluidic fuel cell design avoids many of the issues encountered in polymer electrolyte membrane-based fuel cells [9], including membrane humidification, membrane degradation, and liquid water management. In addition, the co-laminar configuration allows the composition of the anolyte and catholyte streams to be chosen independently [10], thus providing an opportunity to improve reaction rates and cell voltage. Another significant benefit associated with microfluidic fuel cells is cost. Single microfluidic fuel cells can be manufactured by inexpensive, well-established micromachining and microfabrication methods and the cost associated with membrane and auxiliary systems, which is significant for most other fuel cells, is eliminated. Incorporation of this technology in applications will require scale-up, that is, the integration of multiple microfluidic fuel cells, and this has yet to be addressed.

Proof-of-concept microfluidic fuel cells based on vanadium redox species [11], formic acid [12–14], methanol [10,15,16], hydrogen [17–19], and hydrogen peroxide [20] have recently been developed. The majority of these devices employed a single Y- or T-shaped co-laminar microfluidic network featuring fuel and oxidant dissolved in aqueous streams of supporting electrolyte and electrodes placed on opposite channel walls parallel to the inter-diffusion zone. The current density of these fuel cells was primarily restricted by the rate of mass transport to the active sites [21], typically in the cathodic half-cell [15]. For cells using dissolved oxygen in the cathodic stream, the maximum power density reported to date, 5 mW cm^{-2} [10], was predominantly limited by the low solubility of oxygen (2–4 mM). The integration of an air-breathing porous cathode structure allows gaseous oxygen transport from the ambient air, a source of oxygen that has significantly higher diffusivity and concentration than dissolved oxygen. Jayashree et al. [14] developed the first microfluidic fuel cell with integrated air-breathing cathode, using a graphite plate anode covered with Pd black nanoparticles and a porous carbon paper cathode covered with Pt black nanoparticles. Peak power density, 26 mW cm^{-2}, was achieved with 1 M formic acid in 0.5 M sulfuric acid. Air-breathing designs yet require a blank cathodic electrolyte stream with flow rate similar to the anodic stream in order to prevent fuel crossover and facilitate ionic transport between the electrodes. The air-breathing feature also reduces the feasibility of scale-up by three-dimensional stacking of individual cells.

The use of alternative oxidants, soluble at higher concentrations than dissolved oxygen, provides another avenue towards improved performance of mass-transfer limited microfluidic fuel cells. Vanadium redox batteries [22,23] utilize two different aqueous vanadium redox couples, V^{2+}/V^{3+} and VO^{2+}/VO_2^+, as fuel and oxidant, respectively, dissolved in dilute sulfuric acid. This combination of vanadium redox pairs is also suitable for microfluidic fuel cell operation for several reasons: they have high solubility and enable relatively high redox concentrations up to 5.4 M [24]; they provide well-balanced electrochemical half-cells in terms of reaction rates and transport characteristics; they have a large difference in formal redox potentials resulting in a high open-circuit voltage (up to ∼1.7 V at uniform pH) [11]; the reactions are facilitated by plain carbon electrodes that do not require any precious metal catalysts such as Pt or Pd; and the all-vanadium system enables electrolytic regeneration of fuel and oxidant from the used solutions without complex separation schemes. The highest power density of all microfluidic fuel cells published to date, 38 mW cm^{-2}, was achieved using vanadium redox couples [11]. As in other microfluidic fuel cell technologies, however, system integration is challenging, and the energy density is limited by the solubility of the fuel and oxidant.

The power output of a single planar microfluidic fuel cell is inadequate for most practical applications. The feasibility of enlarging a single planar cell, i.e. increasing the geometrical area of electrodes and microchannel, is limited by structural

constraints, increased fuel/oxidant inter-diffusion, and increased ohmic losses if the average distance between anodic and cathodic active sites becomes large. In order to produce adequate power, multiple independent planar cells could be accommodated on a single plane, and then these planes could be stacked as in typical PEM fuel cells. The volumetric power density of such devices would however be limited by the volume of the sealing and structural elements separating the cells. In traditional PEM fuel cell stacks, which are limited by similar issues [25], the bipolar plates serve as structural and electrical components. The inherent advantage of non-planar electrode–electrolyte interfaces has been recognized and demonstrated for such cells using, e.g. waved membrane-electrode assemblies [25]. In contrast, the microfluidic fuel cells presented to date contain mostly non-participating structural material such as glass or poly(dimethylsiloxane) (PDMS). The scale-up of microfluidic fuel cell technology in a volumetrically efficient manner remains a challenge.

The objective of this study is to develop membraneless microfluidic fuel cell architectures employing low-cost graphite rod electrodes. Graphite rod electrodes provide reaction sites and current collection within a single stand-alone structure that requires no additional catalyst or electrode support materials. Experimental as well as numerical and analytical methods are applied to a planar microfluidic fuel cell architecture employing graphite rod electrodes. A three-dimensional microfluidic fuel cell architecture consisting of a hexagonal array of graphite rods is presented. Significant performance gains in terms of both peak power output and fuel utilization are demonstrated with prototypes of both planar and three-dimensional architectures.

2. Experimental

2.1. Microfabrication

2.1.1. Planar cell

A schematic of the planar cell configuration is given in Fig. 1. The cells were manufactured in house, and consist of two layers: a substrate that contains the graphite rod electrodes, and a polymeric top layer that contains the channel structure. Graphite rods were embossed in the base substrate according to the following procedure: a 2 in. × 3 in. microscope glass slide was coated with a 1 mm layer of polyurethane (PMC-790; Smooth-On Inc., Easton, PA) and cured for 2 h on a hot plate at 65 °C. Upon solidification, the polyurethane substrate was placed in an aluminum substrate holder. Two 0.5 mm-diameter graphite rods (Mars micro carbon, type HB; Staedtler, Germany) were fitted in a different custom-made aluminum holder with two parallel grooves that uniformly separated the rods by 1.0 mm and held them in place. The holder was sprayed with universal mold release (Smooth-On Inc.) before use. Both parts were heated on a hot plate to 160 °C and mechanically pressed together to fuse the graphite rods into the softened polyurethane layer. The assembly was removed from the hot plate with the pressure still applied, and allowed to cool down. The aluminum plates were then removed, leaving the graphite rods embossed in the hardened polyurethane layer. The substrate was finished by grinding down the rods to achieve a flush, flat electrode surface. Wires were attached to one end of the rods using conductive epoxy (Circuit Works CW2400; ITW Chemtronics, Kennesaw, GA).

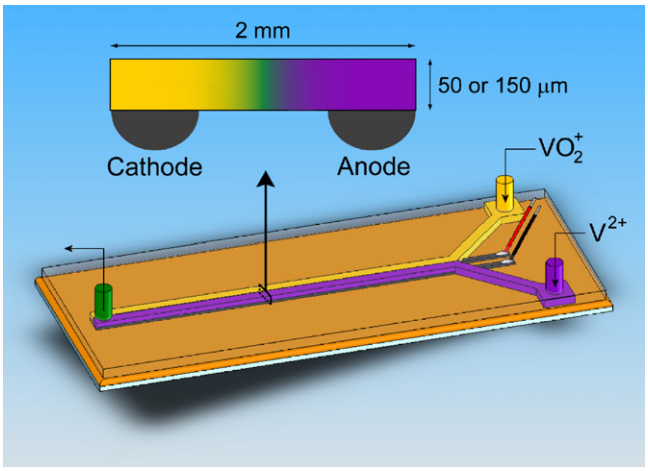

Fig. 1. Schematic of a graphite rod-based microfluidic fuel cell of the planar cell type. The cell employs vanadium redox couples as fuel (V^{2+}, violet) and oxidant (VO_2^+, yellow), shown in representative colors (For interpretation of the references to color in this figure legend, the reader is referred to the web version of the article.).

The top layer of the planar cell, containing the Y-shaped microchannel, was fabricated by replica molding in poly(dimethylsiloxane) (PDMS; Dow Corning, Midland, MI) following established soft-lithographic protocols [26], and process specifics described elsewhere [27]. The channels were 2 mm wide and either 50 or 150 μm high. A master that defines the channel pattern was created by photolithography in negative photoresist (SU-8 50; Microchem, Newton, MA). This structure was cast into a slab of PDMS, which was peeled off the master after curing. Inlet/outlet holes were punched in the PDMS before assembly. The PDMS slab was placed over the polyurethane substrate and the two were aligned precisely under a microscope. While operating the cell, a reversible seal was accomplished by pressing the two parts together with an aluminum clamp. This type of bond allows cleaning of the cell and substitution of the channel structure, such that the substrate may be re-used after each trial. Alternatively, an irreversible seal that does not require clamping can be obtained by plasma-treating the PDMS, which renders hydrophilic channel walls and facilitates covalent binding to the substrate. The electrodes of the assembled fuel cell had a planar active area of 0.165 cm^2 (0.5 mm wide and 33 mm active length). Overall, the above described fabrication procedure is rapid and economical. A set of planar cell units can be fabricated in less than 4 h with a total material cost of US$ 2 per cell.

2.1.2. Three-dimensional array cell

The inherent advantage of non-planar electrode–electrolyte interfaces has, as noted earlier, been recognized before in the context of PEM fuel cell. The array architecture fuel cell proposed here and shown in Fig. 2 uses cylindrical graphite rods as electrodes. This cell comprises of 29 graphite rods mounted inside a 2 mm × 7 mm × 39 mm cavity that was CNC-machined

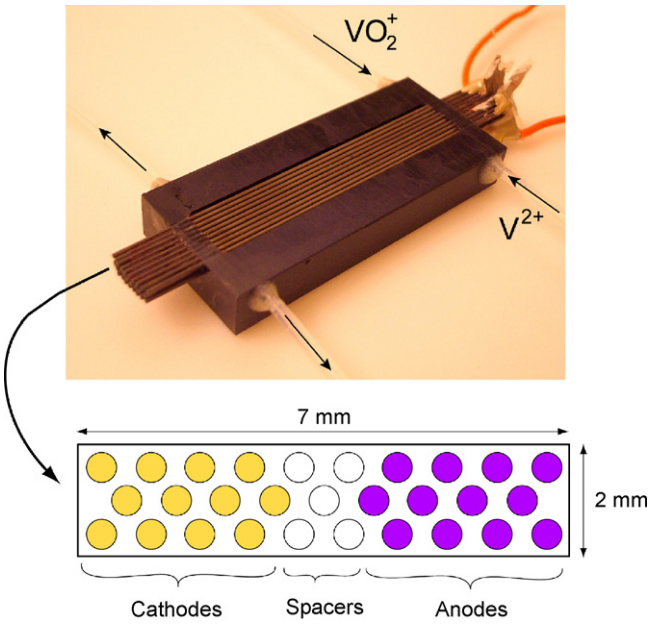

Fig. 2. Three-dimensional vanadium-based microfluidic fuel cell with the array architecture. Graphite rods are mounted in a single CNC-machined cavity. The cell comprises 12 anodes and 12 cathodes that are essentially independent. The five rods in the center of the device are exposed to co-laminar inter-diffusion of anolyte and catholyte and are not electrically connected.

in a 6 mm × 19 mm × 44 mm block of Delrin. Delrin was chosen as it is a heat resistant, inflexible and chemically resilient acetal polymer. To hold and separate the graphite rods, an array of holes in a hexagonal pattern were drilled in the end plates of the cavity. The 0.5 mm diameter graphite rods were fitted in the cavity through the holes and sealed using positive photoresist (SPR 220-7.0; Rohm and Haas, Marlborough, WA). Separate wires were attached to the anodes and cathodes at the end of the rods using conductive epoxy. Inlet and outlet holes were drilled in the sides of the Delrin block and Teflon tubes (Upchurch Scientific, Oak Harbor, WA) were inserted for fluid handling. A thin slab of PDMS formed the top wall of the cavity, and during operation the seal was ensured by an aluminum clamp. The total active area exposed to the fluid was 7.3 cm^2 per electrode.

2.2. Preparation of vanadium solutions

Vanadium-based fuel (V^{2+}) and oxidant (VO_2^+) solutions were prepared according to the following procedure: fresh sulfuric acid supporting electrolyte solution was prepared from Millipore Milli-Q water (Millipore, Billerica, MA) and concentrated sulfuric acid (EMD Chemicals Inc., Gibbstown, NJ). Vanadium sulfate oxide hydrate ($VOSO_4{\cdot}XH_2O$; Alfa Aesar, Ward Hill, MA) was dissolved in the supporting electrolyte by sonication at 50 °C until a clear blue VO^{2+}-solution was obtained. Two different solutions were prepared: 1 M VO^{2+} in 1 M H_2SO_4, and 2 M VO^{2+} in 2 M H_2SO_4.

The required V^{2+} and VO_2^+ solutions were generated from VO^{2+}-solution in an electrolytic flow cell with carbon felt electrodes divided by a Nafion membrane. The VO^{2+}-solution was divided into three equal parts by volume: one part (200 mL) was added to the positive half-cell and the remaining two parts (400 mL) were added to the negative half-cell. Given the instability of the V^{2+} solution in contact with air, it was necessary to continuously purge the negative half-cell with N_2. The solutions were pumped through the cell while applying a fixed electrolytic current of 10 A. The cell voltage was 1.5–1.7 V while charging. Charging was complete after 50 min when the cell voltage quickly rose above 2.0 V, which was also confirmed by the sudden color change in the two compartments. The fully charged purple V^{2+} solution and yellow VO_2^+ solution were removed and stored under an N_2 blanket in air-tight bottles. The current efficiency during charging was calculated to be 99.7%. The use of carbon electrodes ensured that no H_2 or O_2 bubbles were produced during the experiment. The solutions demonstrated high stability under storage for several months with only minor degradation.

The anolyte and catholyte can be regenerated from the mixed (used) solution collected from the outlet(s) of the fuel cells (normally a 50/50 mixture of V^{3+} and VO^{2+} when stabilized) by pouring equal parts into the positive and negative half-cells and repeating the charging procedure.

2.3. Fuel cell diagnostics

The steady co-laminar flow of vanadium solutions required for fuel cell operation was driven by a syringe pump (PHD 2000; Harvard Apparatus, Holliston, MA) via flexible Tygon tubing (planar cell) or Teflon tubing (array cell). Polarization data were obtained at room temperature by chronoamperometry under stepwise potentiostatic control from 0.0 V to open-circuit voltage in 0.1 V increments, using a PARSTAT 2263 potentiostat (Princeton Applied Research, Oak Ridge, TN). The cell current was monitored until steady state was reached, which usually occurred within 120 s. Current densities and power densities for the planar cells reported here are based on the planar active area of the electrodes (0.165 cm^2).

The combined ohmic resistance of the planar cells was evaluated by electrochemical impedance spectroscopy (EIS) using the same potentiostat. An ac amplitude of 5 mV rms was applied over the frequency range from 50 kHz to 0.5 Hz. The ohmic cell resistance was recorded as the high-frequency real axis intercept of the Nyquist plot of impedance. The EIS data were averaged from measurements at four different flow rates (2.5, 10, 60 and 120 μL min^{-1}) using 1 M solutions at 0.5 V cell voltage.

3. Theory

3.1. Numerical current distribution analysis

A primary current distribution model of a 2D cross-sectional plane (Fig. 1) of the co-laminar flow channel was developed for the planar cells in order to quantify in-channel ionic resistance between anode and cathode. The current density ($\vec{J}$) and potential (V) distribution in the channel are coupled and can be solved for simultaneously by considering the electrolyte as a dc conductive medium with electrical conductivity σ governed by

Ohm's law:

$$\vec{J} = -\sigma \nabla V \tag{1}$$

The potential distribution is described by Poisson's equation;

$$-\nabla(\sigma \nabla V) = Q_j \tag{2}$$

where Q_j represents internal current sources. By assuming isotropic conditions, negligible Joule heating (strong convective heat transfer), and no homogeneous reactions ($Q_j = 0$), Eq. (2) turns into the Laplace equation:

$$\nabla^2 V = 0 \tag{3}$$

This governing equation is subject to Neumann boundary conditions (uniform current density normal to the surface) at the anode and cathode surface, and electric insulation at the remaining boundaries (see Fig. 1). The domain was discretized by adaptive meshing and the equations solved for the 2D potential distribution using a direct stationary linear solver available within the commercial software package COMSOL Multiphysics 3.2 (COMSOL Inc., Stockholm, Sweden) under mesh independence control. The total in-channel ohmic resistance was finally obtained by integrating the normalized local current density over the entire domain, i.e.:

$$R_s = \frac{1}{\sigma d^2 l} \int_{A_c} J^{*2} \, dA \tag{4}$$

Here, d and l are the diameter and active length of the graphite rod electrodes, respectively, and the current density (J) is normalized with respect to the current density at the electrodes, J_e, as $J^* = J/J_e$.

3.2. Transport limitation analysis

The theoretical maximum current density of a microfluidic fuel cell, assuming rapid electrochemical reactions, is controlled by the rate of convective/diffusive transport of reactants to the surface of the electrodes. In the transport controlled regime, the boundary condition on the surface of the electrode is defined by zero concentration [28]:

$$c_e = 0 \tag{5}$$

A concentration boundary layer that depends on the flow characteristics will thus develop in the channel, starting at the leading edge of the electrode. To approximate the total flux of reactant to the electrode and sequentially the current, one can consider the limiting case of internal, fully developed laminar flow between two flat plates with one reacting wall, which is a pseudo-3D case that neglects the effects of the side walls of the channel. There is no analytical solution to the described convective/diffusive mass transport problem available in the literature; however, the extensive body of empirical heat transfer correlations may be used together with the heat and mass-transfer analogy to derive approximate scaling laws. The scaling laws employed here were adapted from the analysis provided by Kjeang et al. [29], which focused on the generation of a redox couple at an embedded electrode in a microfluidic channel flow. Only the most relevant details are provided here, and the reader is referred elsewhere [29] for the derivations. The analysis is based on dimensionless scaling of the mean velocity;

$$U^* = \frac{U D_h^2}{l D} \tag{6}$$

where U is the mean velocity, D_h the hydraulic diameter, and D is the diffusion coefficient ($D \approx 10^{-10}$ m^2 s^{-1}). There are two distinct regimes: (i) the high U^* regime, which covers most practical flow rates experienced in microfluidic fuel cells; and (ii) the low U^* regime for low flow rates in channels with small hydraulic diameter. In the high U^* regime, the transport-limited current is proportional to the cubic root of the mean velocity [29]:

$$I = -1.849 F d c_0 \left(\frac{l^2 D^2 U}{D_h} \right)^{1/3} \tag{7}$$

Moreover, the current is proportional to the electrode diameter and the initial vanadium concentration (c_0), and scales as the square of the cubic root of the active length and the inverse cubic root of the hydraulic diameter. This analysis is based on the following assumptions: pseudo-3D momentum and species transport neglecting transverse components, and constant bulk concentration equal to the initial concentration. Alternatively, Eq. (7) can be written in terms of flow rate (Q):

$$I = -1.849 F d c_0 \left(\frac{l^2 D^2 Q}{D_h h w} \right)^{1/3} \tag{8}$$

For high-aspect ratio channels, $D_h \approx 2h$, and the current scales as $h^{-2/3}$ and $w^{-1/3}$ versus the channel height and width, respectively, at constant flow rate. In addition, if we introduce the dimensionless current;

$$I^* = \frac{I}{F d l c_0 D / D_h} \tag{9}$$

we obtain a linear correlation between I^* and $U^{*1/3}$:

$$I^* = -1.849 U^{*1/3} \tag{10}$$

This equation is capable of predicting the transport-limited current independently of initial concentrations and channel geometry within the high U^* regime.

In the low U^* regime, the flux of reactant entering the channel is equal to the rate of the electrochemical reactions, such that all reactant molecules are converted into product species and useful current. We assume that diffusion is strictly two-dimensional and neglect transverse diffusion in the cross-stream direction. In this case, the maximum current is directly proportional to inlet concentration and flow rate [29]:

$$I = -F c_0 Q \tag{11}$$

Again, we can use the dimensionless quantities I^* and U^* to derive a relationship that is valid for high-aspect ratio channels under any conditions within the low U^* regime:

$$I^* = -\tfrac{1}{2} U^* \tag{12}$$

The transition point between the high U^* regime and the low U^* regime occurs at $U^{*1/3} = 1.9$ [29].

4. Results and discussion

4.1. Planar cell operation

A set of planar microfluidic fuel cells, as shown schematically in Fig. 1, were fabricated and vanadium solutions of concentrations 1 and 2 M were freshly prepared using the procedures described in Section 2. Graphite rods, i.e. common mechanical pencil refills that are available off-the-shelf, were used as electrodes without additional catalyst or electrode support materials. Note that small amounts of clays are typically used to bind the graphite in pencil leads; the exact composition depends on hardness and is not supplied by manufacturers.

4.1.1. Open-circuit voltage and redox concentrations

The appropriate anodic and cathodic vanadium redox reactions and standard redox potentials are [30]:

$$V^{3+} + e^- \leftrightarrow V^{2+} \qquad E^\circ = -0.255\ \text{V versus SHE} \tag{13}$$

$$VO_2^+ + 2H^+ + e^- \leftrightarrow VO^{2+} + H_2O \qquad E^\circ = 0.991\ \text{V versus SHE} \tag{14}$$

A fuel cell based on these two half-cell reactions thus has a theoretical reversible cell potential of 1.246 V. Portions of the V^{2+} and VO_2^+ solutions were characterized separately in a three-electrode electrochemical cell with a graphite rod working electrode. The measured open-circuit potentials (OCPs) were −0.317 and 1.116 V (1 M), and −0.309 and 1.192 V (2 M) (versus SHE), respectively. The maximum cell potentials for fuel cell operation based on these solutions are 1.43 V (1 M) and 1.50 V (2 M). By assuming that the open-circuit potentials are reversible potentials, their departure from the standard potentials is related to the solution concentrations by the Nernst equation [31]:

$$E = E^\circ - \frac{RT}{nF} \ln\left(\frac{a_{\text{red}}}{a_{\text{ox}}}\right) \tag{15}$$

In our case, $T = 298$ K, $n = 1$ for both redox pairs, and a is the activity. If we assume equal activity coefficients, the activity ratio can be approximated by the redox concentration ratio. Using this analysis, the following redox concentration ratios were obtained: 92% V^{2+}/8% V^{3+} and 99.2% VO_2^+/0.8% VO^{2+} (1 M); 89% V^{2+}/11% V^{3+} and 99.8% VO_2^+/0.2% VO^{2+} (2 M). These highly biased concentration ratios explain the enhanced cell potentials measured here. The cell potential can be increased beyond 1.50 V by the use of high-purity vanadium solutions, e.g. Ferrigno et al. [11] achieved 1.67 V with approximately 99.9% VO_2^+/0.1% VO^{2+} and 99.9% V^{2+}/0.1% V^{3+} concentration ratios at 1 M.

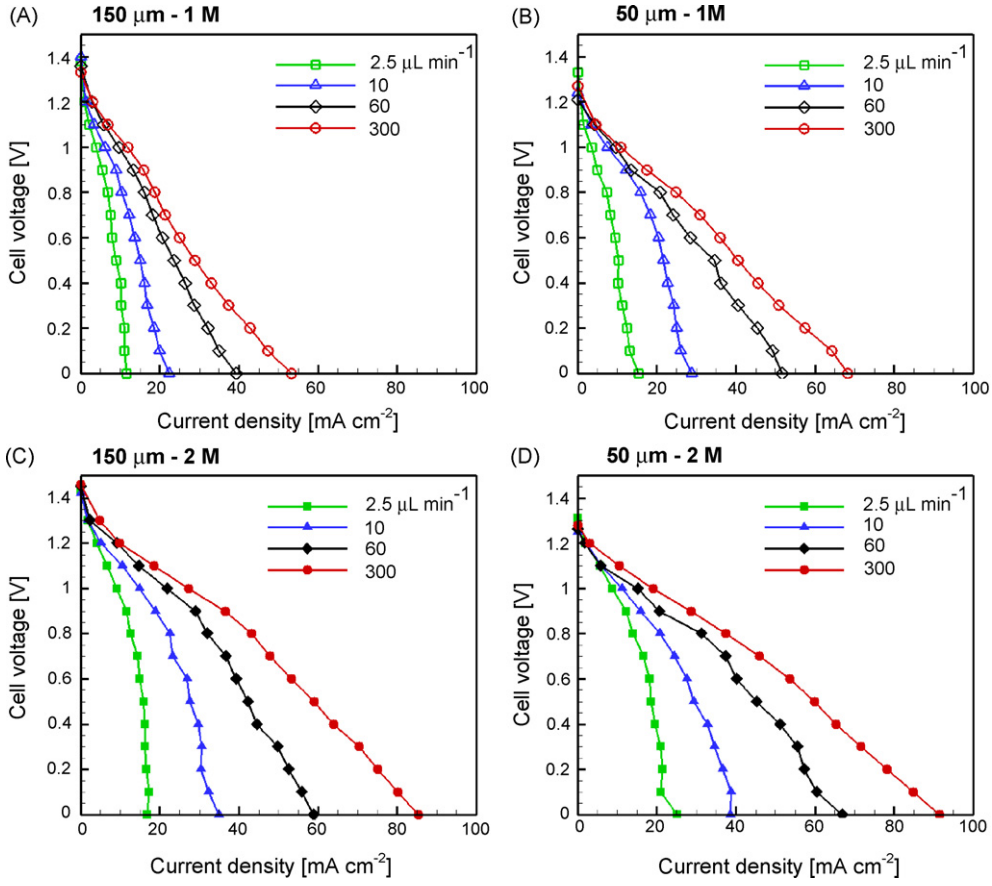

Fig. 3. Experimentally determined polarization curves for the planar cells using 1 M (A and B) and 2 M (C and D) vanadium solutions in 150 μm (A and C) and 50 μm (B and D) high microfluidic channels. The legend indicates flow rate per stream.

4.1.2. Polarization

The performance of the planar cell architecture was evaluated for four different combinations of channel height and vanadium concentration: (i) 150 μm and 1 M; (ii) 150 μm and 2 M; (iii) 50 μm and 1M; (iv) 50 μm and 2 M. Polarization data were measured by chronoamperometry under potentiostatic control at steady state conditions. The amperometric measurements were remarkably steady and predictable with an initial current peak as the cell potential was applied that decreased continuously over time towards the steady state current. Furthermore, repeated trials showed highly reproducible trends with an average standard deviation of less than 2%. The polarization data were reproducible under galvanostatic control, indicating that the same internal conditions are established independently of the control method. The planar cells were successfully operated at flow rates spanning four orders of magnitude. Fig. 3 shows polarization data at flow rates between 2.5 and 300 μL min^{-1} per stream. The open-circuit voltages measured in the fuel cells were 1.19–1.41 and 1.24–1.46 V for 1 and 2 M solutions, respectively. Although 1–17% less than the values measured in the electrochemical cell, these open-circuit voltages are significantly higher than those possible in methanol/oxygen or hydrogen/oxygen fuel cells [30]. The obtained values were generally higher for the 150 μm channel height than for the thinner 50 μm channel. The polarization trends at low flow rates show typical signs of mass-transfer limitations as the cell voltage drops quickly at a limiting current. The impact of mass-transfer limitations from the bulk solution is reduced by enhanced convective transport at high flow rates, as indicated by the increasing current densities at higher flow rates. At 300 μL min^{-1}, for example, there was no indication of bulk transport limitations. The slope of the polarization curves is steadier at high flow rates, which indicates that the produced current was limited by a combination of ohmic resistance, faradaic electrochemical impedance, and species transport to and from the active sites. Given the same flow rate, the convective velocity in the 50 μm channel was triple that in the 150 μm channel. The result of the increased velocity was a thinner diffusion layer and higher maximum current density, particularly in the case of 1 M solutions. A more quantitative analysis of these transport effects is provided through the transport limitation analysis in Section 4.1.6. The highest current density produced was 92 mA cm^{-2} at 300 μL min^{-1} and 2 M vanadium solutions.

4.1.3. Power density

The corresponding power density data shown in Fig. 4 were obtained by multiplying the current density by the cell voltage. The most prominent effect identified here is the strong dependence of power density on both flow rate and vanadium concentrations. These results indicate that the power output of these devices is primarily controlled by transport characteristics and that the electrochemical reactions are relatively

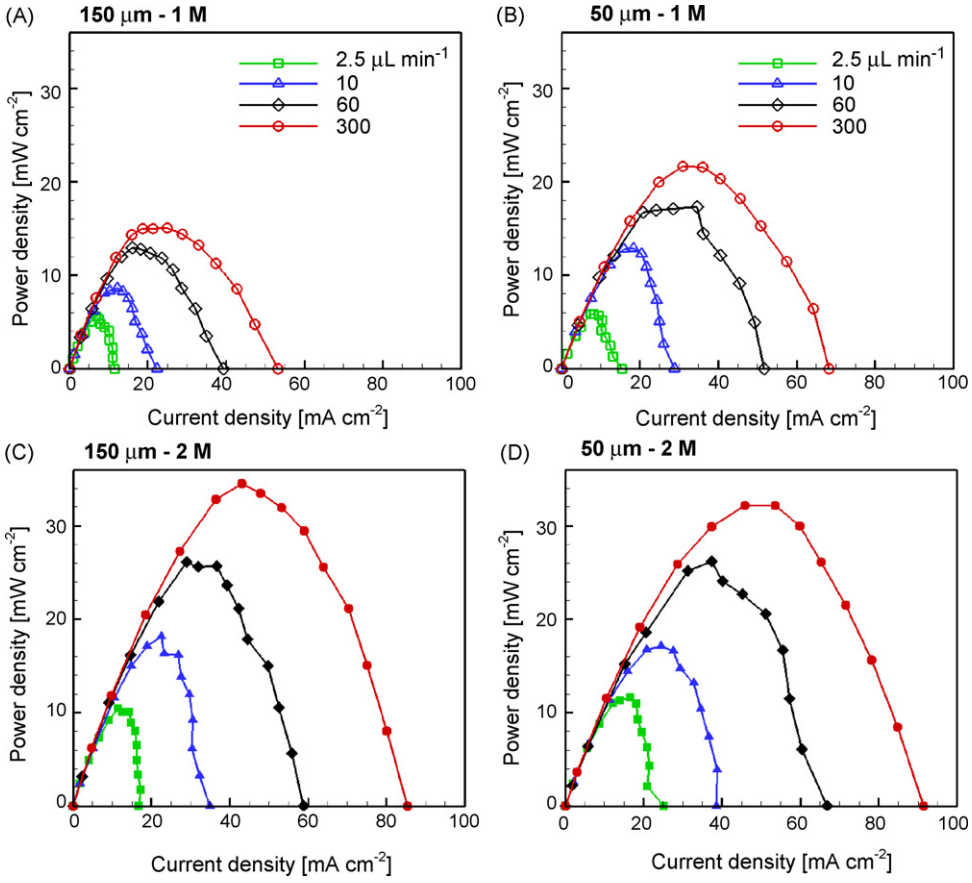

Fig. 4. Power density curves for planar cell operation using 1 M (A and B) and 2 M (C and D) vanadium solutions in 150 μm (A and C) and 50 μm (B and D) high microfluidic channels, based on the polarization data in Fig. 3. The legend in A and B indicates flow rate per stream, also representative for C and D.

fast. In the context of the evaluation of graphite rods as carbon microfluidic fuel cell electrodes, this is an encouraging result.

Peak power was generally achieved within a cell voltage range of 0.6–0.9 V, which can be considered a competitive range compared to most other types of fuel cells. The highest peak power density in this study, 35 mW cm^{-2} at 0.8 V, was obtained for the 150 μm cell at the highest flow rate (300 μL min^{-1}) and 2 M vanadium concentrations. This level of power density is similar to that of previous vanadium-based microfluidic fuel cells [11] although the flow rate used here was only 1/5 as high. Moreover, this power density is 35–100% higher than air-breathing cells [14,16] and seven times higher than the best cells based on dissolved oxygen [10].

Points of peak power density for each curve are plotted for comparison in Fig. 5A versus the logarithm of the flow rate. It is noteworthy that the 150 μm cell was capable of reaching higher peak power densities than the 50 μm cell at high flow rates of 2 M vanadium, despite lower maximum current densities. This feature is attributed to the higher open-circuit voltage measured for the larger channel, which indicates superior electrochemical characteristics and larger electromotive force. The effect of channel height is nevertheless more dominant at 1 M concentrations, where the 50 μm cell performs significantly better than the 150 μm cell. In addition, the improvements in power density upon switching from 1 to 2 M vanadium are much larger for the 150 μm cell than the 50 μm cell; at 300 μL min^{-1}, for example, the peak power of the 150 μm cell was enhanced by 230% compared to a mere 49% for the 50 μm cell. The difference between the two cells is related to the stronger convective transport experienced by the 50 μm cell, as will be discussed further in Section 4.1.6. The continuous slope of peak power density versus flow rate shown for all cases in Fig. 5A demonstrates the ability to tune the flow rate to satisfy unsteady power requirements of applications. The response time of the fuel cell to a transient duty cycle is expected to be on the order of 1–10 s, depending on the flow rate regime.

The pumping power required to sustain steady co-laminar flow in high-aspect ratio channels can be estimated based on laminar flow theory as the pressure drop multiplied by the flow rate according to Ref. [32]:

$$W = \Delta p Q = \frac{32\mu l Q^2}{w h D_h^2} = \frac{8\mu l Q^2}{w h^3} \quad (16)$$

By neglecting the pressure drop associated with inlet channels and off-chip tubing as well as other losses, and using the dynamic viscosity (μ) for water, the pumping power required for the highest flow rate and smallest channel under study becomes $W \approx 20$ μW. This power requirement is less than 1% of the power output of the fuel cell, and can therefore be neglected.

4.1.4. Fuel utilization

The coulombic single pass fuel utilization is defined as the current output divided by the flux of reactant entering the channel:

$$\eta = \frac{I}{n F c_0 Q} \quad (17)$$

The geometry of the planar cells is well suited to achieve high fuel utilization at low flow rates. Specifically, the mixing interface between the streams is perpendicular to the electrode surfaces, and the high-aspect ratio ensures that the electrode area is large compared to that of the mixing interface [7]. This configuration limits inter-diffusive fuel/oxidant crossover, thereby enabling operation at low-range flow rates and high fuel utilization. The maximum single pass fuel utilization obtained for the planar cells is presented in Fig. 5B as a function of flow rate for all cases under study. As expected, the fuel utilization was maximized for the lowest flow rates, and decreased with flow rate. The moderate penalty in power density associated with the transition to low flow rates (Fig. 5A), from ~30 down to ~10 mW cm^{-2}, is offset by a large boost in fuel utilization from ~1 to ~40%. The highest fuel utilization obtained here was 63% (1 M, 2.5 μL min^{-1}, 50 μm). This level is remarkably high: the highest fuel utilization presented to date for other microfluidic fuel cells was 33% [14], although the fuel utilization levels at practical flow rates and cell voltages were typically less than 1%. Highly practical operational characteristics in terms of both power density and fuel utilization were achieved here, in particular with the 50 μm cell operating at 2.5 μL min^{-1} with

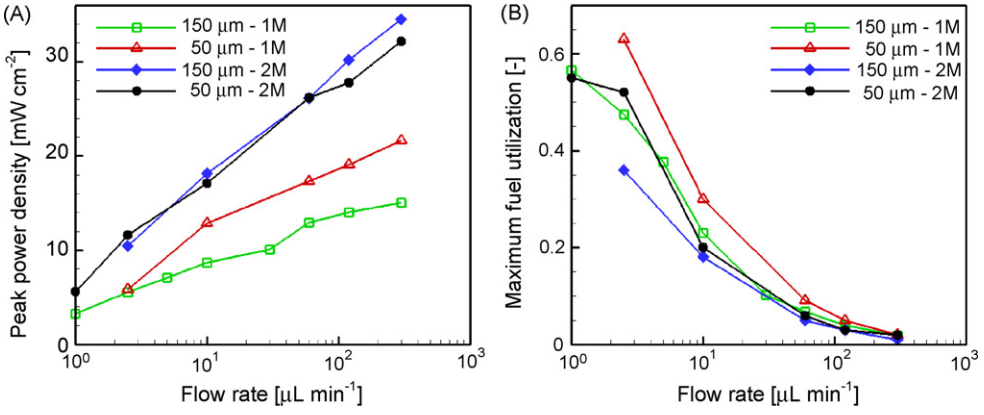

Fig. 5. Experimental results of peak power density (A) and maximum fuel utilization (B) for planar cells with different channel heights and vanadium concentrations (indicated in the legend), plotted vs. the logarithm of the flow rate per stream.

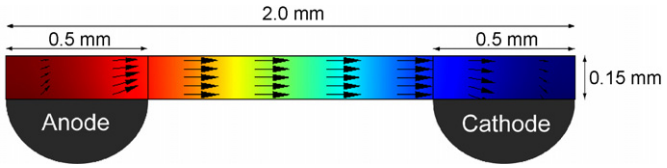

Fig. 6. Numerically determined electrical potential distribution inside the microfluidic channel of a single cell (obtained from the primary current distribution model). Red and blue colors represent high and low electrical potentials, respectively, and the arrows show the current distribution facilitated by ionic transport (For interpretation of the references to color in this figure legend, the reader is referred to the web version of the article.).

2 M vanadium. This configuration enabled a power density of 11 mW cm^{-2} at 0.6 V combined with a single pass fuel utilization of 38%.

4.1.5. Ohmic resistance

The ohmic resistance in the channel is proportional to the average charge transfer distance between anode and cathode, which can be approximated by the following scaling law:

$$R_S = \frac{s}{\sigma h l} \tag{18}$$

Since the inter-electrode spacing (s) is relatively large (1 mm), ohmic resistance in microfluidic fuel cells is generally higher than in membrane-based fuel cells. One way to reduce ohmic resistance is to increase the concentration of the supporting electrolyte. For example, the conductivity of dilute sulfuric acid increases from 35 S m^{-1} for 1 M to 58 S m^{-1} for 2 M concentration at 25 °C [30]. A primary current distribution model that essentially considers the channel a 2D electrostatic conductor was developed (Section 3.1) in order to obtain a prediction of the total ohmic resistance in the flow channel of the planar cells with geometry shown in Fig. 1. The results obtained for the 150 μm cell are given in Fig. 6: the normalized ionic current distribution between anode and cathode is shown by the arrows; and the normalized electrical potential distribution is shown in the background, with red and blue colors representing high and low electrical potential, respectively. The electrical potential distribution modeled here is induced by ohmic resistance, and is partly contributing to the losses in electrochemical cell potential. The total in-channel ohmic resistance was integrated using Eq. (4) for the two planar cell geometries studied here. Electrochemical impedance spectroscopy was performed experimentally to estimate the overall ohmic resistance of the cell. This measurement includes contributions from in-channel ionic resistance as well as electrical series resistance introduced by electrodes, contacts and wires. The results from the scaling analysis, the current distribution model and the EIS investigation are compared in Table 1. As expected, the scaling law underestimates the in-channel resistance compared to the results obtained by the current distribution model, which includes the effects of electrode and cell geometry. The difference between the results from the model and the EIS study indicate the magnitude of the additional electrical series resistance component included in the EIS results. The ohmic resistance of the graphite rods was ~3 Ω per electrode, as measured with a multimeter across a 60 mm long individual rod, which only constitutes a fraction of the overall resistance measured by EIS. The majority of the ohmic resistance is therefore associated with ionic charge transport in the channel and external electrical contacts. Interestingly, the EIS results were very similar for both channel heights, unlike those obtained by the current distribution model. Given the large difference between EIS and model results for 150 μm, we believe that the resistances measured by EIS are dominated by the electrical contact resistance component, and that the agreement between EIS and model results for 50 μm is serendipitous. The in-channel resistance should therefore be much smaller than predicted by the other methods. This inevitably raises the question whether or not the charge transfer mechanism proposed here is entirely valid for this type of microfluidic fuel cells. It is possible, for instance, that some local depletion or accumulation of ions masks the in-channel ohmic resistance. A thorough EIS investigation of these phenomena is currently under development by our group.

Table 1
Ohmic resistance of planar cells with channel height h and 1 M vanadium solutions, obtained by the scaling law (Eq. (18)), the primary current distribution model (Eq. (4)), and electrochemical impedance spectroscopy (EIS)

h (μm)	Scaling (Ω)	Model (Ω)	EIS (Ω)
150	6	8	22
50	17	23	24

4.1.6. Transport limitation analysis

Scaling laws for the convective/diffusive transport-limited current density were presented in Section 3.2. Two transport regimes were identified: the low U^* regime and the high U^* regime, based on the dimensionless mean velocity given in Eq. (6). The transport-limited current is proportional to the flow rate in the low U^* regime and scales as the cube root of the flow rate in the high U^* regime. The maximum current densities measured experimentally for the 150 μm planar cell with 1 M solutions are compared to the scaling laws in Fig. 7A. In this case, the maximum current density follows the scaling laws very closely in both flow regimes, except at the highest flow rate (300 μL min^{-1}). This operating case is therefore predominantly limited by convective transport from the bulk fluid, rather than any reaction kinetics associated with graphite rod based electrodes. Fig. 7B shows experimental data for all four cases studied here, plotted together using the dimensionless quantities I^* and $U^{*1/3}$ to represent maximum current density and mean velocity, respectively. Using these variables, the scaling curves in both U^* regimes collapse into a single function, which is linear above the transition point to the high U^* regime at $U^{*1/3} = 1.9$. The experimental currents are entirely transport-limited at low flow rates for all cases. At high flow rates, however, the transport-limitation is generally not reached. This effect may be explained as follows: the rate of convective transport increases with flow rate, vanadium concentration and inverse channel height. As convective transport becomes stronger (see Fig. 7B), demand on the electrochemical and electrical aspects of the cell increases, and thus effects of non-ideal reaction kinetics and ohmic resistance become sig-

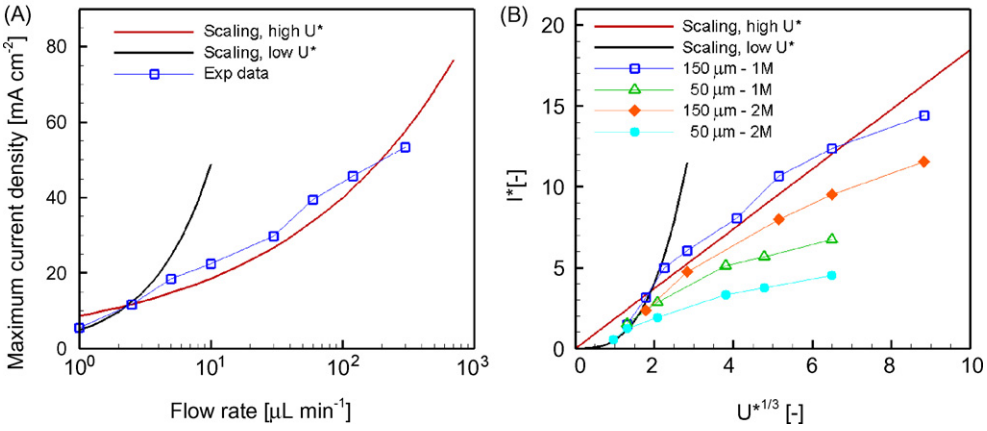

Fig. 7. Transport limitation analysis: (A) maximum current density measured experimentally for a planar cell with 1 M vanadium concentrations and 150 μm channel height, and (B) for different vanadium concentrations and channel heights based on dimensionless variables for maximum current density (I^*) and flow rate ($U^{*1/3}$). Also plotted are the empirical scaling laws for the transport-limited cases at high and low U^*.

nificant. This is especially noticeable in the 50 μm cell which experiences the highest velocities for a given flow rate. In these cases, the current is not strictly transport limited, but is controlled by a combination of factors related to transport, electrochemistry and ohmic resistance. In sum, the current density was predominantly limited by convective/diffusive transport as opposed to reaction kinetics. The ability to reach transport-limited operation over a wide range of flow rates demonstrates the viability of graphite rod electrodes as core fuel cell components.

4.2. Array cell operation

Three-dimensional array architecture fuel cells with design shown in Fig. 2 were fabricated according to the procedure described in Section 2.1.2. The array cell design is based on 29 graphite rods of 0.5 mm diameter assembled inside a single cavity. The average spacing between the rods was 200 μm, and thus the flow characteristics within the available space are microfluidic in nature and similar to those of the planar cells. Although the inter-diffusion zones located in between the central rods in the array cell are non-planar, the width of these inter-diffusion zones is expected to grow at a similar rate as for the planar cells. To compensate for the inter-diffusion zone, the five central rods are electrically insulated (see Fig. 2). This inter-diffusion zone is flanked by 12 individual anodes and 12 individual cathodes. For the purposes of this study, all 12 electrodes of each type were connected in parallel. This simple configuration enabled performance comparison with the planar cells; however, alternative electrode connection combinations are numerous. The array architecture inherently provides many more options with respect to power conditioning than a conventional stack. Conceivably electrode connections could be made dynamically via control electronics in response to load, and thus enable dynamic power conditioning at the fuel cell level. With respect to scalability, the array cell configuration may be readily expanded in both vertical (preferable) and horizontal directions to increase capacity. Scale-up of these cells requires only an enlarged cavity, in contrast to the volumetric costs of additional substrates and fluid delivery networks associated with stacking planar cells.

4.2.1. Open-circuit voltage and redox concentrations

The V^{2+} and VO_2^+ solutions utilized for the array cell were similar to the 1 M solutions used in the planar cell study except for the redox concentration ratios. The open-circuit potentials, measured in a three-electrode electrochemical cell, were −0.272 and 1.061 V (versus SHE). The maximum cell potential for fuel cell operation based on these solutions is 1.33 V. Using the Nernst equation, Eq. (15), the following redox concentration ratios were obtained: 64% V^{2+}/36% V^{3+} and 94% VO_2^+/6% VO^{2+}. The feed concentration was therefore limited to 0.64 M.

4.2.2. Polarization

Polarization data were measured for the array cell according to the procedure previously described for planar cell operation. Fig. 8A shows polarization data at flow rates between 10 and 2000 μL min^{-1} per stream, plotted as cell voltage versus current. Also plotted for comparison are the results of planar cell operation at 300 μL min^{-1} (150 μm channel and 1 M vanadium). The open-circuit voltages measured in the array cell ranged from 0.84 V at 10 μL min^{-1} to 1.36 V at 2000 μL min^{-1}. This increasing trend is attributed to the more uniform solution distribution encountered at high flow rates. Operation at flow rates less than 10 μL min^{-1} was found to be impractical due to the sharp drop in cell voltage induced by increased inter-diffusion and non-uniform flow. The cross-sectional flow area in the bundle is about 30 times larger than the 150 μm planar cell, and the mean convective velocity is therefore 30 times less at a fixed flow rate. The overall shape of the polarization curves are similar to the ones measured for the planar cells, and as before, some transport limitation behavior is apparent at lower flow rates. However, the currents obtained with the array cell are notably higher than for planar cell operation at the same flow rate. The maximum current measured here was 86 mA at 2000 μL min^{-1}.

4.2.3. Power output

The power curves obtained experimentally for array cell operation are shown in Fig. 8B together with the power curve generated by the 150 μm planar cell (at 300 μL min^{-1} and 1 M). The array cell produced more power than the planar cell at all

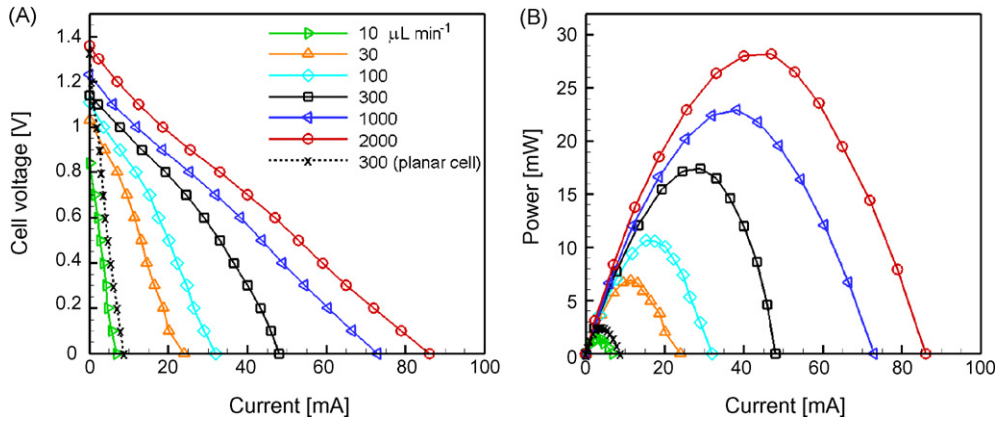

Fig. 8. Polarization (A) and power (B) curves obtained experimentally for array cell operation at flow rates per stream as indicated, using 0.64 M vanadium solutions. The data are compared to planar cell operation using 1 M solutions at 300 μL min^{-1} flow rates in a 150 μm high channel.

flow rates above 10 μL min^{-1}, and its power output increased substantially with flow rate. Fig. 9A presents peak power as a function of logarithmic flow rate for the array cell and planar cell. At a fixed flow rate of 300 μL min^{-1}, the array cell produced seven times more power (17.4 mW) than the planar cell (2.5 mW). This is considered an appropriate performance comparison, given that the 'cost' in terms of fuel and oxidant supply is identical. The array cell also operated effectively at low flow rates; for example, the array cell produced 6.9 mW at 30 μL min^{-1}, which is nearly three times more than the planar cell could produce at 300 μL min^{-1}, a 10 times higher flow rate.

The highest power output measured for the array cell was 28 mW at 0.6 V and 2000 μL min^{-1}. Based on the total active area of the array cell, this power level is equivalent to a moderate power density of 3.8 mW cm^{-2}. This relatively low power density compared to those of the planar cells is attributed to several factors: the significantly lower V^{2+} concentration (0.64 M); the higher in-channel ohmic resistance; the non-uniform flow distribution; and most importantly, the lower convective velocity at fixed flow rate.

In the context of a fuel cell stack, volumetric power density is a more relevant metric. For the array cell, the volumetric power density based on the entire volume of the cavity was 52 mW cm^{-3}. Though this volumetric power density is nominally higher than for the planar cells at 1 M, a direct comparison is ambiguous at this stage since no attempt has been made to quantify and minimize the "overhead" volumes of supporting infrastructure (i.e. walls, substrates and fluid manifolds). Suffice it to state that the proof-of-concept three-dimensional cell with its uniquely scalable array architecture demonstrated an order of magnitude higher power output than the planar design.

4.2.4. Fuel utilization

The maximum coulombic single pass fuel utilization of the array cell is shown in Fig. 9B as a function of the logarithmic flow rate, and compared to planar cell operation (150 μm and 1 M). The array cell is capable of reaching higher fuel utilization levels than the planar cells due to its reduced relative inter-electrode spacing. The highest fuel utilization obtained by the array cell was 78%, which is remarkably high. In addition, at any given flow rate above 30 μL min^{-1}, the fuel utilization capability of the array cell was approximately one order of magnitude higher than for the planar cell. Practical operational characteristics were identified at 30 μL min^{-1}; at this flow rate, the array cell produced 6.6 mW at 0.5 V combined with 43% single pass fuel utilization. Fuel-efficient array cell operation at low-

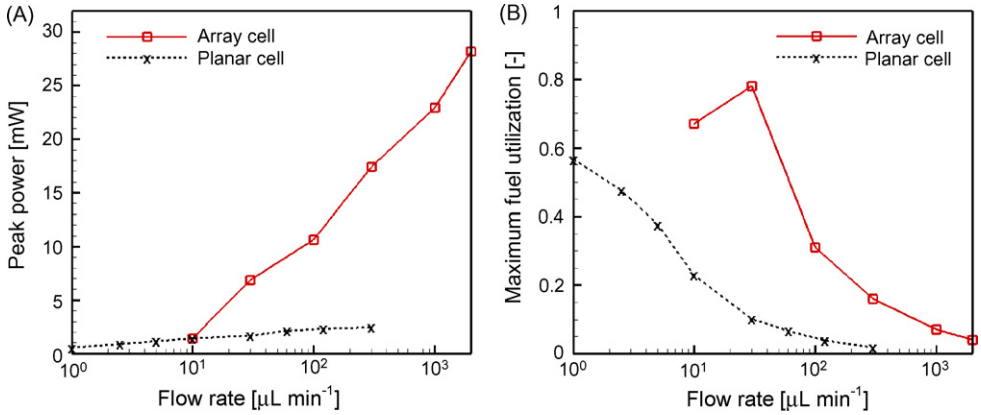

Fig. 9. Peak power (A) and maximum fuel utilization (B) determined experimentally for array cell operation using 0.64 M vanadium concentrations, compared to that of the planar cell with 1 M vanadium concentrations and 150 μm channel height. The data are plotted vs. the logarithm of the flow rate per stream.

range flow rates is a key finding for future research in this field: as microfluidic fuel cell technology transitions from proof-of-concept planar cell structures to integrated three-dimensional architectures with multiple cells, fuel utilization becomes an increasingly important parameter.

5. Conclusions

New membraneless microfluidic fuel cell designs were demonstrated based on graphite rod electrodes. Low-cost graphite rods, available as mechanical pencil refills, provided both reaction sites and current collectors for the combined all-vanadium fuel and oxidant system without additional catalyst requirements. Planar single cells, comparable to existing fuel cell designs, were manufactured and evaluated experimentally to confirm the viability of the proposed graphite rod electrodes. Planar cell operation was demonstrated for flow rates spanning four orders of magnitude with a maximum power density of 35 mW cm^{-2}. Empirical transport analysis verified that the performance was primarily restricted by convective/diffusive transport from the bulk. Particularly effective planar cell operation was shown at low flow rates, achieving unprecedented levels of fuel utilization up to 63% per single pass.

Unlike film-deposited electrodes, graphite rod electrodes enable unique three-dimensional array cell integration. Our proof-of-concept three-dimensional microfluidic fuel cell architecture, based on a hexagonal array of graphite rods, produced an order of magnitude more power than the planar cell at similar flow rates. Furthermore, highly efficient array cell operation was demonstrated at low to moderate flow rates, achieving even higher fuel utilization than the planar cell. The array cell, with multiple anodes and cathodes, provides great power conditioning flexibility in series and/or parallel configurations, as well as unique scalability by vertical expansion without additional fluid manifold requirements or performance loss. We expect that fuel cell performance would further benefit from increasing the concentration and purity level of both supporting electrolyte and vanadium redox species, and by optimizing the rod diameter and characteristic spacing of the array cell.

Acknowledgments

The funding for this research provided by a Natural Sciences and Engineering Research Council (NSERC) strategic grant and by Angstrom Power Inc. is highly appreciated. The authors would also like to thank Dr. Clive Brereton and Evan Hobenshield at NORAM Engineering and Constructors Ltd. for experimental support.

References

[1] C.K. Dyer, J. Power Sources 106 (2002) 31–34.
[2] G. McLean, N. Djilali, M. Whale, T. Niet, 10th Canadian Hydrogen Conference, Quebec City, QC, Canada, 2000.
[3] N.T. Nguyen, S.H. Chan, J. Micromech. Microeng. 16 (2006) R1–R12.
[4] E. Kjeang, J. Goldak, M.R. Golriz, J. Gu, D. James, K. Kordesch, Fuel Cells 5 (2005) 486–498.
[5] G.Q. Lu, C.Y. Wang, T.J. Yen, X. Zhang, Electrochim. Acta 49 (2004) 821–828.
[6] S. Wasmus, A. Kuver, J. Electroanal. Chem. 461 (1999) 14–31.
[7] A. Bazylak, D. Sinton, N. Djilali, J. Power Sources 143 (2005) 57–66.
[8] R.F. Ismagilov, A.D. Stroock, P.J.A. Kenis, G. Whitesides, H.A. Stone, Appl. Phys. Lett. 76 (2000) 2376–2378.
[9] S. Litster, D. Sinton, N. Djilali, J. Power Sources 154 (2006) 95–105.
[10] E.R. Choban, J.S. Spendelow, L. Gancs, A. Wieckowski, P.J.A. Kenis, Electrochim. Acta 50 (2005) 5390–5398.
[11] R. Ferrigno, A.D. Stroock, T.D. Clark, M. Mayer, G.M. Whitesides, J. Am. Chem. Soc. 124 (2002) 12930–12931.
[12] E.R. Choban, L.J. Markoski, A. Wieckowski, P.J.A. Kenis, J. Power Sources 128 (2004) 54–60.
[13] J.L. Cohen, D.A. Westly, A. Pechenik, H.D. Abruna, J. Power Sources 139 (2005) 96–105.
[14] R.S. Jayashree, L. Gancs, E.R. Choban, A. Primak, D. Natarajan, L.J. Markoski, P.J.A. Kenis, J. Am. Chem. Soc. 127 (2005) 16758–16759.
[15] E.R. Choban, P. Waszczuk, P.J.A. Kenis, Electrochem. Solid State Lett. 8 (2005) A348–A352.
[16] R.S. Jayashree, D. Egas, J.S. Spendelow, D. Natarajan, L.J. Markoski, P.J.A. Kenis, Electrochem. Solid State Lett. 9 (2006) A252–A256.
[17] J.L. Cohen, D.J. Volpe, D.A. Westly, A. Pechenik, H.D. Abruna, Langmuir 21 (2005) 3544–3550.
[18] S.M. Mitrovski, L.C.C. Elliott, R.G. Nuzzo, Langmuir 20 (2004) 6974–6976.
[19] S.M. Mitrovski, R.G. Nuzzo, Lab Chip 6 (2006) 353–361.
[20] S. Hasegawa, K. Shimotani, K. Kishi, H. Watanabe, Electrochem. Solid State Lett. 8 (2005) A119–A121.
[21] M.H. Chang, F. Chen, N.S. Fang, J. Power Sources 159 (2006) 810–816.
[22] M. Rychcik, M. Skyllaskazacos, J. Power Sources 22 (1988) 59–67.
[23] M. Skyllaskazacos, F. Grossmith, J. Electrochem. Soc. 134 (1987) 2950–2953.
[24] W. SkyllasKazacos, C. Menictas, M. Kazacos, J. Electrochem. Soc. 143 (1996) L86–L88.
[25] W.R. Merida, G. McLean, N. Djilali, J. Power Sources 102 (2001) 178–185.
[26] D.C. Duffy, J.C. McDonald, O.J.A. Schueller, G.M. Whitesides, Anal. Chem. 70 (1998) 4974–4984.
[27] J.T. Coleman, J. McKechnie, D. Sinton, Lab Chip 6 (2006) 1033–1039.
[28] R.F. Probstein, Physicochemical Hydrodynamics—An Introduction, John Wiley and Sons, Inc., Hoboken, NJ, 2003.
[29] E. Kjeang, B. Roesch, J. McKechnie, D.A. Harrington, N. Djilali, D. Sinton, Microfluid. Nanofluid., doi:10.1007/s10404-006-0128-1.
[30] D.R. Lide (Ed.), CRC Handbook of Chemistry and Physics, 83rd ed., CRC Press, Boca Raton, FL, 2002.
[31] J. Newman, K.E. Thomas-Alyea, Electrochemical Systems, third ed., John Wiley & Sons, Inc., Hoboken, NJ, 2004.
[32] E. Kjeang, D. Sinton, D.A. Harrington, J. Power Sources 158 (2006) 1–12.